

Check for updates

# Robust Superlinear Photoresponse Based on p-Te/n-MoS<sub>2</sub> Van Der Waals Heterojunction

Lijian Li, Peng Guo, Kai Tang, Shulin Sha, Tong Xu, Peng Wan, Caixia Kan, Daning Shi,\* Xiaosheng Fang,\* and Mingming Jiang\*

Photodetectors exhibiting robust superlinear photoresponse characteristics can overcome the limitations of traditional devices whose figures-of-merits decrease with increasing light irradiance at high levels, thereby providing a significant breakthrough for the development of intelligent optical devices with low power consumption and high efficiency. Herein, a p-Te/n-MoS<sub>2</sub> van der Waals heterojunction photodetector is experimentally achieved that exhibits self-powering operation, fast response speed, broadband, and polarizationsensitive photodetection. When exposed to 570 nm illumination at 0 V bias, the detector demonstrates excellent performance, including a responsivity of 74 mA  $W^{-1}$ , a specific detectivity of 4.1  $\times$  10<sup>10</sup> Jones, fast rising/falling times of 35/34 µs and a high photocurrent anisotropy ratio of 1.85. The device maintains competitive photodetection properties upon intense lights in comparison with its competitors, which is attributed to its superlinear photoresponse. Specifically, its superlinear photoresponse value reaches up to 2.0 at 254 nm, while it also showcases outstanding superlinear values in the broadband response regions. Associated with theoretical analysis, the superlinear photoresponse is primarily attributed to the photogating layer mechanism of 1D Te single crystals and their excellent hole conduction capability. This study paves the way for creating high-performance photodetectors with potential applications in highresolution imaging, spectral analysis, neuromorphic networks, and others.

1. Introduction

Photodetectors have the ability to convert optical signals into electrical signals, making them crucial for potential fields such as

L. Li, P. Guo, K. Tang, S. Sha, T. Xu, P. Wan, C. Kan, D. Shi, X. Fang, M. Jiang

College of Physics

MIIT Key Laboratory of Aerospace Information Materials and Physics Key Laboratory for Intelligent Nano Materials and Devices

Nanjing University of Aeronautics and Astronautics

Nanjing 211106, P. R. China

E-mail: shi@nuaa.edu.cn; xshfang@fudan.edu.cn; mmjiang@nuaa.edu.cn

Department of Materials Science and State Key Laboratory of Molecular **Engineering of Polymers Fudan University** 

Shanghai 200438, P. R. China

The ORCID identification number(s) for the author(s) of this article can be found under https://doi.org/10.1002/adfm.202420359

DOI: 10.1002/adfm.202420359

clean energy, imaging, communication, environmental monitoring, and biosensing.[1-4] The majority of researchers are striving for the miniaturization and high performance of optoelectronic devices through material optimization and device architecture design.[5-11] For fully functional optoelectronic chips, the development of exploring photodetector components with high photoresponse under intense light is indispensable for achieving the transmission of critical electrical signals in photonic circuits.[12] When operated under high-power conditions, semiconductor materials readily approach the critical point of saturation absorption and the interior of the device is also severely affected by thermal effects.[13] These unfavorable factors would deteriorate the device's performance, or even lead to irreversible damage, which causes a lot of critical bottlenecks that are hindering their continuous and efficient operation. The newly-reported photodetectors, which exhibit superlinear photoresponse, not only convert the absorbed photons into a superlinearly increased photoresponsivity

but also effectively distribute and dissipate excess energy through various physical mechanisms such as thermal dissipation and ion-phonon scattering at high-level of light irradiance.[14] The multifaceted energy utilization and allocation strategy can effectively regulate and mitigate the potential damage to photodetectors caused by excessive incident optical power, thereby ensuring long-term stable operation and performance optimization of the system. It has the potential to break through the linear response limitations of existing photodetectors to intense lights at large optical power densities, further enhancing the intensity and processing capabilities of photoelectric signals.[15]

Recently, the photodetectors with superlinear photoresponse characteristics derived from working mechanisms like second-harmonic generation (SHG) upconversion,[16,17] photo thermionic effect, [18,19] carrier-defect trapping, [20-22] and inverse Auger recombination, [23] have been experimentally and theoretically exhibited. For the SHG upconversion and photothermionic effect, the unique physical properties of the required materials and the complex design of the device structures have caused many obstacles in the pursuit of superlinear photoresponse. Meanwhile, the physical process of carrier-defect trapping

16163208, 0, Downloaded from https://advanced.onlinelibrary.wiley.com/doi/10.1002/adfm.022420359 by Fudau University. Wiley Online Library on [06/03/2025]. See the Terms and Conditions (https://onlinelibrary.wiley.com/terms-and-conditions) on Wiley Online Library for rules of use; OA articles are governed by the applicable Creative Commons License

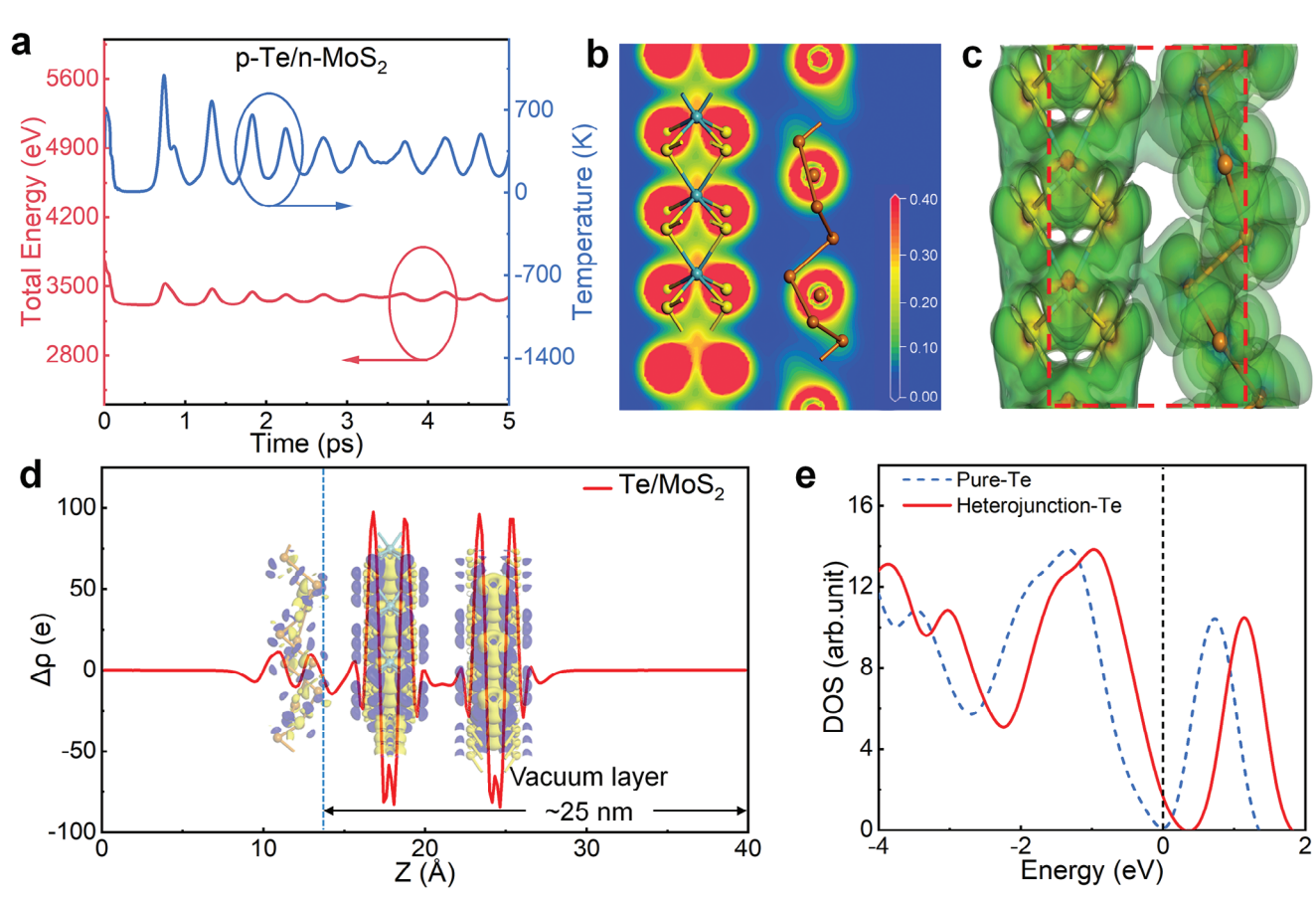


Figure 1. Theoretical calculation of carrier dynamics for  $Te/MoS_2$  structures. a) The temperature (right axis) and the total energy (left axis) as a function of time during MD simulation of the  $Te/MoS_2$  model at 300 K. b) Charge density of  $Te/MoS_2$  model. c) Electrostatic potential of the  $Te/MoS_2$  model. d) The differential charge density of the  $Te/MoS_2$  interface. e) Calculated DOS extracted from the  $Te/MoS_2$  model (red line).

involves a series of complex interactions, making it challenging to determine the functional relationship between the responsivities and optical powers. Regarding the reverse Auger recombination, it typically exhibits inefficient superlinear photoresponse characteristics, posing significant challenges for the practical application of devices. Therefore, exploring photodetectors with broadband spectral range and robust superlinear photoresponse is crucial for achieving efficient reception and processing of high-power optical signals.<sup>[24]</sup>

In this work, we have constructed a p-Te/n-MoS<sub>2</sub> van der Waals heterojunction (vdWH) photodetector, which allowed us to achieve self-driving operational manner, broadband detection, excellent polarization-sensitive, ultrafast response speed. The strong interlayer coupling, dangling-free bond nature, and enhanced charge transfer at the Te/MoS<sub>2</sub> junction interface have been investigated in detail by Kelvin probe force microscopy, Raman spectroscopy, photoluminescence, and electrical measurements. More importantly, the superlinear photoresponse that is closely related to the incident wavelength has been observed in the p-Te/n-MoS<sub>2</sub> vdWH photodetector. This study opens up exciting engineering opportunities for future applications of photodetector capable of operating at high power levels.

### 2. Result and Discussion

The linearity of photoresponse in traditional Te-based optoelectronic devices is often limited by their poor light absorption and fast photocarrier recombination. Manipulating such ultrafast interband and intraband recombination rates is a crucial prerequisite for the practical application of Te-based materials and optoelectronic devices. In this regard, atomic-scale simulations of Te and Te/MoS<sub>2</sub> structure are performed based on density functional theory. To verify the kinetic stability of the Te/MoS<sub>2</sub> structure, ab initio molecular dynamics (MD) simulations are computed at 300 K. The total energy and temperature remain near constant values with very small fluctuations (Figure 1a), confirming the thermodynamic stability of the Te/MoS2 structure. The charge density can effectively identify the interactions between these materials. In Figure 1b, the effective overlap of charge density between Te and MoS<sub>2</sub> is  $<1.00 \times 10^{-1}$  e Å<sup>-3</sup>, which implies that they are bonded by vdW interaction.<sup>[25]</sup> The electrostatic potential at the interface allows for qualitative analysis of the electronic state between Te and MoS2, with red (electrophilic) and blue (nucleophilic) regions representing high and low electron density, respectively. The electrostatic potential distribution at the Te/MoS<sub>2</sub> interface in Figure 1c is relatively uniform, with the Te atom appearing light blue, and the Mo and S atoms appearing

16163028, 0, Downloaded from https://advanced.onlinelbtarry.wiley.com/doi/10.1002/adfm.020420359 by Fudau University, Wiley Online Library on [06/03/2025]. Sether Terms and Conditions (https://onlinelibrary.wiley.com/terms-and-conditions) on Wiley Online Library for uses: OA arctices are governed by the applicable Creative Commons Licenses

www.afm-journal.de

orange-red. The results show that nucleophilic Te is more susceptible to electron transfer reactions with electrophilic MoS<sub>2</sub> in a vdW contacting manner. In this case, the Te atoms can act as electron donors during their interaction. Furthermore, the differential charge density diagram provides a more intuitive depiction of the distribution of electrons and holes within the Te and MoS<sub>2</sub> layers. In the figure, the blue area represents electron accumulation, while the yellow area represents electron depletion. Figure 1d shows that electrons are mainly transferred from the Te layer to MoS<sub>2</sub> in the Te/MoS<sub>2</sub> structure. The density of states (DOS) profiles of pure Te and Te layers extracted from Te/MoS<sub>2</sub> heterojunction structure are compared. The Fermi levels of Te in heterojunction structure are shifted to the valence band compared to pure Te (Figure 1e). It indicates that in the Te/MoS<sub>2</sub> structure, electrons can be considered to accumulate near the Te layer, making it equivalent to a negative charge center. More importantly, the self-hole doping in Te crystals possesses the capability to alter the relative position of the Fermi level, which serves as a crucial mechanism for achieving efficient trapping of photocarriers.[26,27]

Currently, the Te single crystals (SCs) obtained using physical vapor deposition (PVD) methods inherently exhibit hole doping with a typical carrier density in the order of 10<sup>16</sup> cm<sup>-3</sup>, which is consistent with previous reports on samples grown using similar methods. [28,29] Previous studies have shown that the defective state of the self-assembled photogating layer on the surfaces of Te SCs has a significant effect on the gain upon light irradiation with different wavelengths.[30] Upon light illumination, these surface defects trap the generated photocarriers and continuously form gate electric fields, which enable to modulation the channel conductance. The resulting process leads to the collection of more photoinduced electron-hole pairs by the electrodes, which translates to a higher gain in the device. [31,32] Based on the above analysis, the utilization of Te/MoS2 heterojunction structure to construct optoelectronic devices with superlinear photoresponse characteristics is conceptually and technically

Experimentally, the sample of 1D Te SCs with high-quality, size-controlled, and well-defined structures are grown using a simple PVD method in a dual-zone tube furnace, as illustrated in **Figure 2a.** In the synthesis, the precursor Te powder ( $\approx$ 99.99%) is placed in the high-temperature zone (450 °C) at the inlet of the inner tube after being fully ground and mixed. Pure Ar gas is utilized as the carrier gas to transport the precursor vapor at a flow rate of 50 sccm. The SiO<sub>2</sub>/Si substrates are positioned in the low-temperature zone (345 °C) at the outlet of the inner tube. As the synthesis is accomplished, the product of 1D Te SCs with lengths of several hundred µm and widths of tens of µm can be observed on the substrates, as typically shown in the bright-field optical microscope image in Figure 2b. The crystal structure of Te with hexagonal structure is shown in Figure S1a (Supporting Information). Within each molecular chain, the Te atom is strongly covalently bonded to two adjacent atoms along the long axis, with the adjacent atoms rotated by 120°, forming an infinite triangular helix. X-ray diffraction measurements are performed to determine the crystal structure, where the prominent diffraction peaks match well with the standard PDF card (PDF#36-1452) for 1D Te SCs (Figure S1b, Supporting Information). As shown in Figure S1c (Supporting Information), a very homogeneous distribution of the measured heights of the samples is achieved using atomic force microscopy. The PVD-synthesized 1D Te SCs exhibit no organic residues on their surfaces, which are distinguished from the samples synthesized by hydrothermal methods.[33] Thereby, the product of 1D Te SCs with high crystallinity is experimentally obtained. High-resolution transmission electron microscopy analysis reveals the lattice spacing of Te SCs: 3.85 Å, which corresponds to the (100) plane (Figure S2, Supporting Information). The Raman spectrum in Figure 2c displays three main peaks at 93, 121, and 141 cm<sup>-1</sup>, which are in good agreement with the  $E_1$ ,  $A_1$ , and  $E_2$  phonon modes of  $\beta$ -Te crystals.[34] The peak at 93 cm<sup>-1</sup> corresponds to asymmetric stretching of atoms along the a-axis, while the peak at 141 cm<sup>-1</sup> arises from asymmetric stretching along the c-axis direction. The A<sub>1</sub> peak belongs to the chain-extension mode, attributed to the motion of atoms within the basal plane.

The in-plane anisotropic properties of 1D Te SCs are characterized using a confocal Raman microscope system. As shown in Figure 2d,e, strong in-plane vibrational anisotropy is evident in both parallel and orthogonal configurations. To visualize the anisotropy in the Raman spectra of 1D Te SCs, Raman peaks are separated and plotted in polar coordinates at different rotation angles. The Raman peak intensities of the E<sub>1</sub> and E<sub>2</sub> modes undergo significant periodic variations in both parallel and orthogonal configurations as the sample rotation angle changes. In the orthogonal polarization configuration (Figure 2f), the variation periods of the  $E_1$  and  $E_2$  peaks are  $2\pi$  and  $\pi$ , respectively. In the parallel polarization configuration (Figure 2g), the E<sub>1</sub> Raman peak exhibits a variation period of  $\pi$ , while the E<sub>2</sub> Raman peak has a period of  $\pi/2$ . Combined, these results reveal a strong anisotropic crystal structure for the PVD-synthesized 1D Te SCs, which offers potential for the development of advanced polarization-sensitive photodetectors.

The 1D Te SCs and mechanically exfoliated MoS2 layers are sequentially transferred onto the SiO<sub>2</sub>/Si substrate using a dry transfer process, thus giving rise to a vertical stack of layered materials (Figure S3, Supporting Information). After exfoliation, the multi-layer  $MoS_2$  has a lower defect concentration and a flat atomic surface without unsaturated dangling bonds, which ensures its compatibility with 1D Te SCs. Figure 3a displays the three-dimensional diagramming of the well-proposed device structure. Here, scanning electron microscope (SEM) and energy dispersive X-ray spectroscopy reveal that the interface at the overlapping region of the Te/MoS2 structure is exceptionally clean (Figure 3b; Figure S4, Supporting Information), devoid of any impurities or residues. It provides favorable conditions for the efficient transport of photocarriers. The Raman spectroscopy enables to characterize the quality of the Te/MoS<sub>2</sub> structure (Figure S5, Supporting Information). Upon a 532 nm laser excitation, two prominent peaks at 385 and 410 cm<sup>-1</sup> are respectively corresponding to the in-plane  $E_{2,g}$  mode and out-of-plane  $A_{1,g}$  mode of MoS<sub>2</sub>. [35] Notably, no significant shifts could be observed in any of the characteristic peaks. The overlapping region of the Te/MoS<sub>2</sub> structure exhibits typical Te and MoS2 peaks, companied by the quenched intensities of the MoS2 peaks. The quenching behavior of Raman intensity is attributed to two factors: i) the shielding effect of the upper Te reducing the laser intensity captured by the underlying MoS<sub>2</sub>; ii) interlayer charge transfer between Te and  $MoS_{2}$ .[36]

16163028, 0, Downloaded from https://advanced.onlinelibrary.wiley.com/doi/10.1002/adfm.202420359 by Fudan University, Wiley Online Library on [06/03/2025]. See the Terms and Conditions (https://onlinelibrary.wiley.com/terms

and-conditions) on Wiley Online Library for rules of use; OA articles are governed by the applicable Creative Commons License

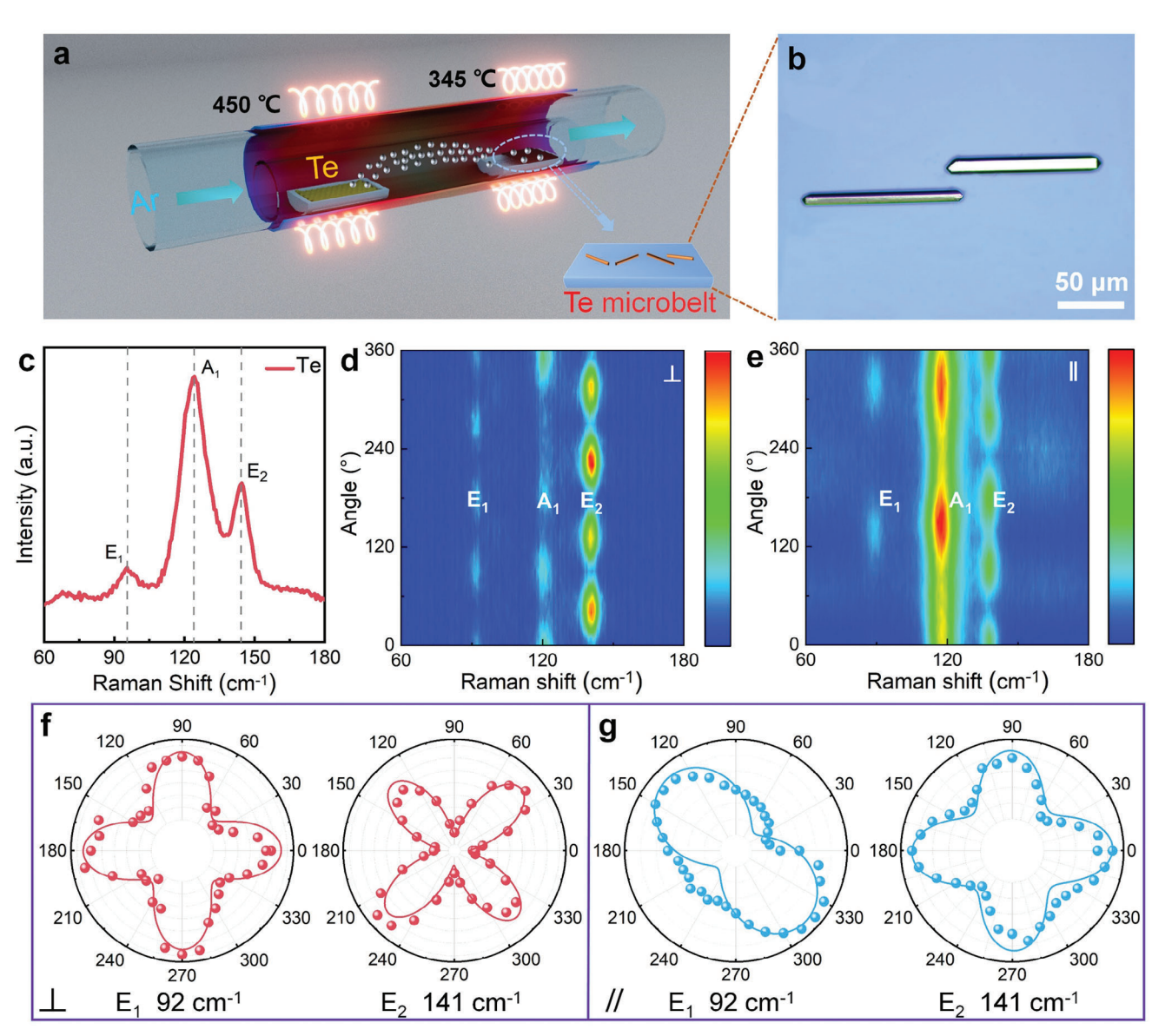


Figure 2. Growth and characterizations of Te SCs. a) Schematic structure illustrating the growing process of low-dimensional Te SCs. b) Optical microscopy image of Te sample. c) Raman spectra of Te. Contour color maps of Raman spectra as a function of the rotation angle of Te under d) orthogonal and e) parallel polarization configurations. Corresponding polar plots for the Raman intensity of  $E_1$ , and  $E_2$  modes with angle under f) orthogonal and g) parallel polarization configurations, respectively.

The Kelvin probe force microscopy (KPFM) is the potentially preferred method for determining the surface potential of layered materials. It can generate work function differences with good spatial resolution. The use of KPFM allows to analysis of fluctuations in interface potentials. Figure 3c presents the surface potential measured by KPFM upon contact between Te and MoS<sub>2</sub>, revealing a contacting potential difference of ≈61 mV. Photoluminescence (PL) spectroscopy can effectively investigate the dynamic behavior of photocarriers. Figure 3d shows the collected PL intensities of the Te SC, the MoS<sub>2</sub> layer, and the hybrid Te/MoS<sub>2</sub> structure, respectively. A dominant peak centered at 1.79 eV (≈691 nm) is observed in MoS<sub>2</sub>. Compared to the pristine MoS<sub>2</sub>, the hybrid Te/MoS<sub>2</sub> heterostructure undergoes a significant intensity quenching. It suggests that a built-in elec-

tric field could be formed in the stacked region at the Te/MoS $_2$  heterointerface, resulting in considerable charge transfer. The optoelectronic properties of the Te/MoS $_2$  heterostructure are taken into account. Since the photocurrent of the Te/MoS $_2$  device is primarily contributed by MoS $_2$ , the photoresponse cutoff wavelength is  $\approx 700$  nm. The wavelength-dependent photocurrent curve in Figure 3e exhibits a broadband photoresponse, enabling the Te/MoS $_2$  photodetector to detect lights ranging from the solar-blind to the visible spectrum. As depicted in Figure 3f, three representative wavelengths (254, 405, and 570 nm) are selected within this range, and the corresponding output curves under illumination and dark conditions are tested. The Te/MoS $_2$  device exhibits a sensitive photoresponse under constant power ( $\approx 5.0~{\rm mW~cm^{-2}}$ ). In darkness, the photodetector generates an

16163028, 0, Downloaded from https://advanced.onlinelibrary.wiley.com/doi/10.1002/adfm.202420359 by Fudan University, Wiley Online Library on [06/03/2025]. See the Terms and Conditions (https://onlinelibrary.wiley.com/terms

-and-conditions) on Wiley Online Library for rules of use; OA articles are governed by the applicable Creative Commons License

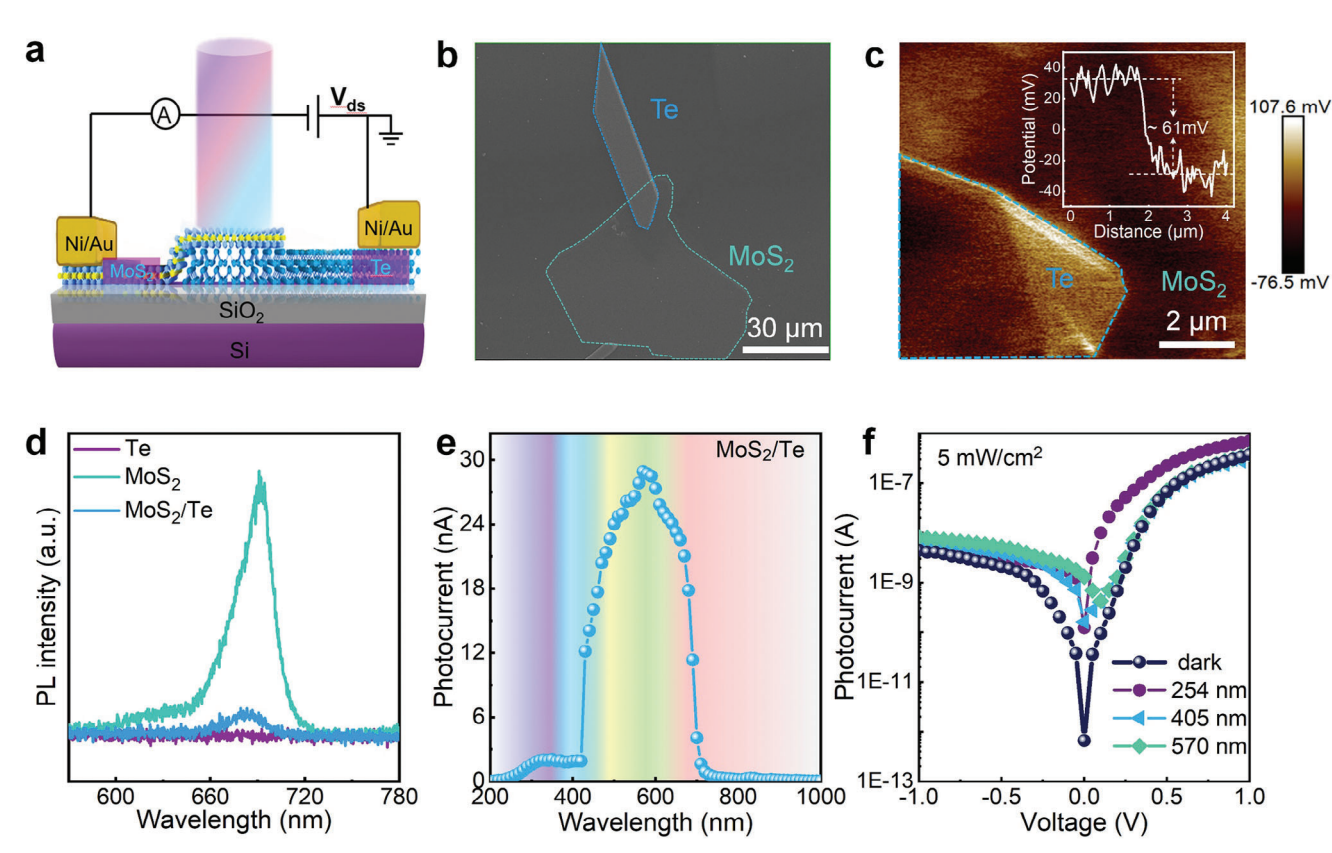


Figure 3. Characterization of Te/MoS<sub>2</sub> photodetector. a) Schematic diagram of the device under light irradiation. b) SEM of the Te/MoS<sub>2</sub> photodetector. c) The surface potential difference of the Te/MoS<sub>2</sub> photodetector. d) PL spectra of MoS<sub>2</sub>, Te, and the related Te/MoS<sub>2</sub> structure. e) Light wavelengthrelated photocurrent ranging from 200–1000 nm when operated at V = 0 V. f) I-V curves of the device plotted in the dark and under illumination at light wavelengths of 254, 405, and 570 nm ( $P = 5.0 \text{ mW cm}^{-2}$ ).

ultra-low dark current of  $6.63 \times 10^{-13}$  A at 0 V bias. The plotted I-V curve shows a typical asymmetric current illustrating a strong built-in electric field at the junction. The device shows a clear photoresponse under different lighting. In the realm of practical photodetectors, spectral responsivity (R) plays a pivotal role as it denotes the device's efficacy in converting incoming light signals into electrical signals. As two other important performance parameters of the photodetector, the noise equivalent power (NEP) and detectivity  $(D^*)$  are affected by the three main types of noise, Johnson noise, 1/f noise, and shot noise from dark current. R and  $D^*$  can be evaluated using the following formulas:

$$R = \frac{I_{ph} - I_d}{PS} \tag{1}$$

$$NEP = \frac{\sqrt{\langle I_n^2 \rangle}}{R}$$
 (2)

$$D^* = \frac{\sqrt{S\Delta f}}{\text{NEP}} \tag{3}$$

where  $I_{\rm ph}$ ,  $I_{\rm d}$ , P, S,  $I_{\rm n}^2$ , and  $\Delta f$  represent the photocurrent, dark current, laser power density, active area ( $\approx 5.596 \times 10^{-6} \text{ cm}^{-2}$ ), noise current power, and bandwidth, respectively. The relevant noise power density spectrum of Te/MoS2 vdWH is shown in Figure \$6 (Supporting Information). The relationships between the calculated R and  $D^*$  values and optical intensity at the three wavelengths are extracted from the *I*–*t* curves under various light irradiances (Figure S7a-c, Supporting Information). As shown in Figure 4a-c, the highest responsivities evaluated at 254, 405, and 570 nm are 5.9, 19, and 74 mA W<sup>-1</sup>, respectively; while the relating highest  $D^*$  values are  $3.2 \times 10^9$  Jones,  $1.0 \times 10^{10}$  Jones, and  $4.1 \times 10^{10}$  Jones, respectively. The observed sharp increase in R with increasing optical power, contrary to intuition, suggests that the Te/MoS2 vdWH has a higher optoelectronic efficiency. The unusual phenomenon is explained in more detail below.

The relationship between the normalized photocurrents and the modulation frequency is shown in Figure 4d, where the amplitude of the photocurrent decreases with an increase in the modulation frequency. The observed 3 dB bandwidth demonstrates that the cutoff frequency, where the photocurrent decays to 0.707 times its initial stable value, is determined to be 4.5 kHz. Figure 4e displays the temporal response of the fabricated devices to pulsed illumination tested at different frequencies of 0.1, 2.5, and 4 kHz, respectively. Thereby, the Te/MoS<sub>2</sub> photodetector has a fast and stable response. By zooming in on the periodic curve at 4 kHz (Figure 4f), the response time (35 µs) and decay time (34 µs) of the device are extracted, which surpass most reported Te-associated photodetectors via the

www.afm-journal.de

16163028, 0, Downloaded from https://advanced.onlinelbtarry.wiley.com/doi/10.1002/adfm.020420359 by Fudau University, Wiley Online Library on [06/03/2025]. Sether Terms and Conditions (https://onlinelibrary.wiley.com/terms-and-conditions) on Wiley Online Library for uses: OA arctices are governed by the applicable Creative Commons Licenses

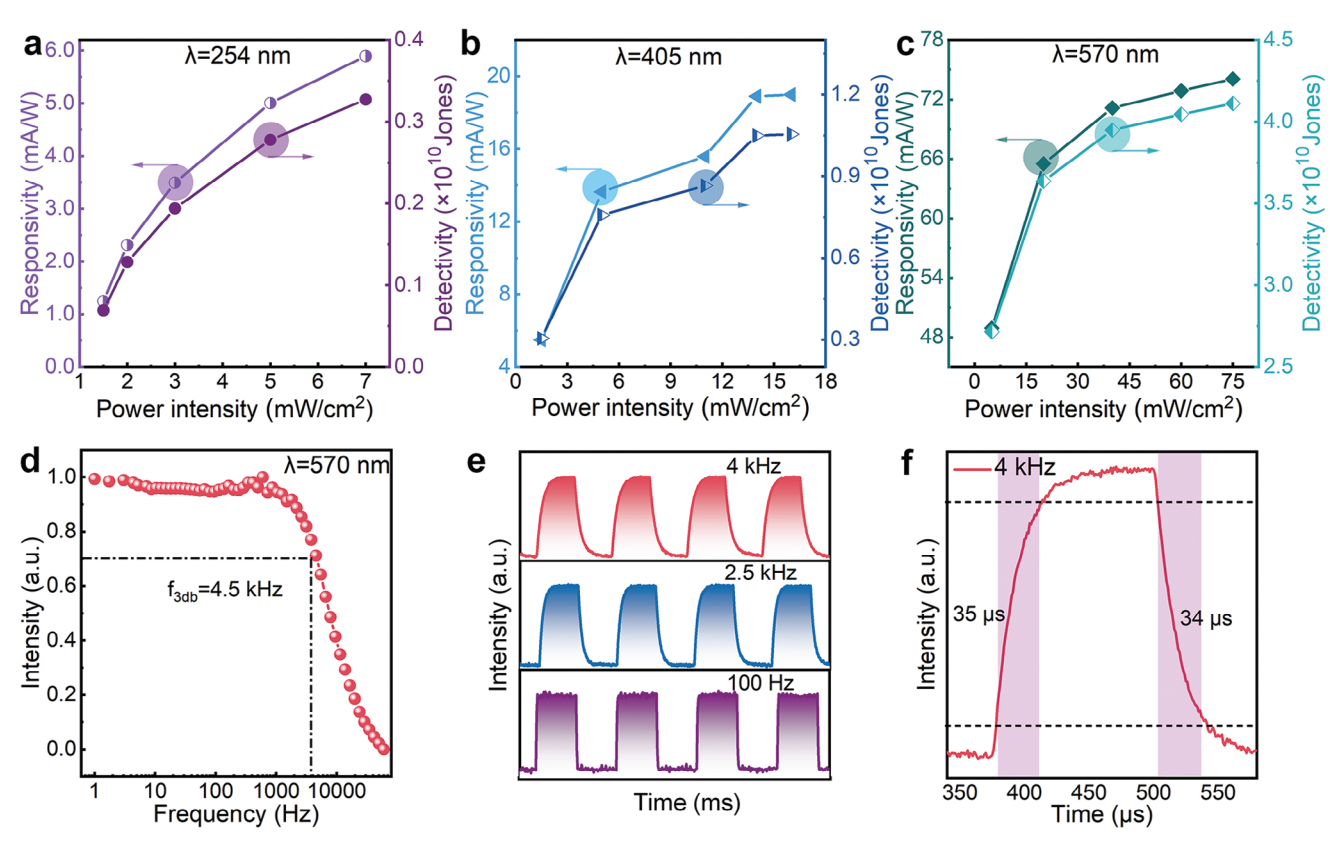


**Figure 4.** Photoresponse properties of the as-constructed p-Te/n-MoS<sub>2</sub> photodetector. Light irradiance-dependent R and  $D^*$  of the Te/MoS<sub>2</sub> detector when evaluated at the wavelengths of a) 254, b) 405, and c) 570 nm, respectively. d) Normalized intensity of photocurrent as a function of the modulation frequency. e) Photoresponse properties of the device to pulsed light (570 nm) at different frequencies of 0.1, 2.5, and 4 kHz. f) The response speed was evaluated by measuring photocurrent over time at a chopper frequency of 4 kHz.

photovoltaic effect.[39-41] The Te/MoS<sub>2</sub> vdWH photodetector maintains excellent photoresponse characteristics after exposure to air for 6 months (Figure S8, Supporting Information), indicating good environmental stability. The superior performance of the device can be attributed to the following factors: i) The highquality Te/MoS2 contact interface ensures a low concentration of defects and traps at the interface. This significantly inhibits the recombination of photocarriers and leads to high responsivity and detectivity. ii) The built-in electric field at the Te/MoS<sub>2</sub> interface facilitates rapid separation of photogenerated electronhole pairs. The vertically stacked device structure provides a fast path for carrier transport, contributing to an improved response speed. iii) The Te is proven to be a "Weyl semiconductor" with coexisting Weyl cones and bandgaps, where carriers can exhibit high mobility, thus contributing to the ultrafast and substantial photoresponse.[42,43]

In addition to the discussion of photodetector performance, an unusual phenomenon is observed in the light irradiance-dependent photocurrents, which exhibit superlinear behavior at different wavelengths of photoexcitation. Figure 5a-c show the light irradiance-dependent I-V curves of the  $Te/MoS_2$  vdWH under illumination at wavelengths 254, 405, and 570 nm, respectively. To better understand the phenomenon, the photocurrent is described as a function of incident light intensity and fitted using the formula  $I_{ph} \propto P^{\alpha}$ . When plotted in the double logarithmic in Figure 5d-f, the fitted slopes between the current density gen-

erated by the three excitation wavelengths and the laser power densities exhibit superlinear behavior. The resulting exponents  $\alpha$  are evaluated to 2.03  $\pm$  0.08, 1.54  $\pm$  0.03, and 1.23  $\pm$  0.01 for the excitation wavelengths of 254, 405, and 570 nm, respectively. The values of  $\alpha$  in this paper are all exceeding 1.0, and even reach 2.0, indicating that the light irradiance-dependent photocurrents of the Te/MoS2 vdWH detector exhibit significantly superlinear characteristics. In this case, the device's photoresponse exhibits a considerable increase with increasing optical power densities of incoming lights. The superlinear feature, which is dependent on light irradiances, is distinguished from the sublinear behavior observed in exfoliated MoS2 optoelectronic devices (Figure S9, Supporting Information). It is worth noting that electrodes exhibit good ohmic contact with Te, while MoS2 shows a slight Schottky contact (Figure \$10, Supporting Information). Compared to the strong built-in electric field at the Te/MoS<sub>2</sub> interface, the Schottky barrier at the electrode contact can be neglected. In addition, the Te/MoS2 vdWH detector constructed using 1D Te nanowire also exhibited wavelength-dependent superlinear photoresponse behavior (Figure S11, Supporting Information). Conclusively, the Te/MoS<sub>2</sub> vdWH detector has good fidelity, reliability, and reproducibility.

The working principle of superlinearity-related photoresponse is analyzed as follows. The surface state defects in 1D Te SCs are situated above the conduction band energy level. When the photon energy of the incoming lights exceeds the threshold

16163028, 0, Downloaded from https://advanced.onlinelibrary.wiley.com/doi/10.1002/adfm.202420359 by Fudan University, Wiley Online Library on [06/03/2025]. See the Terms and Conditions (https://onlinelibrary.wiley

on Wiley Online Library for rules of use; OA articles are governed by the applicable Creative Commons L

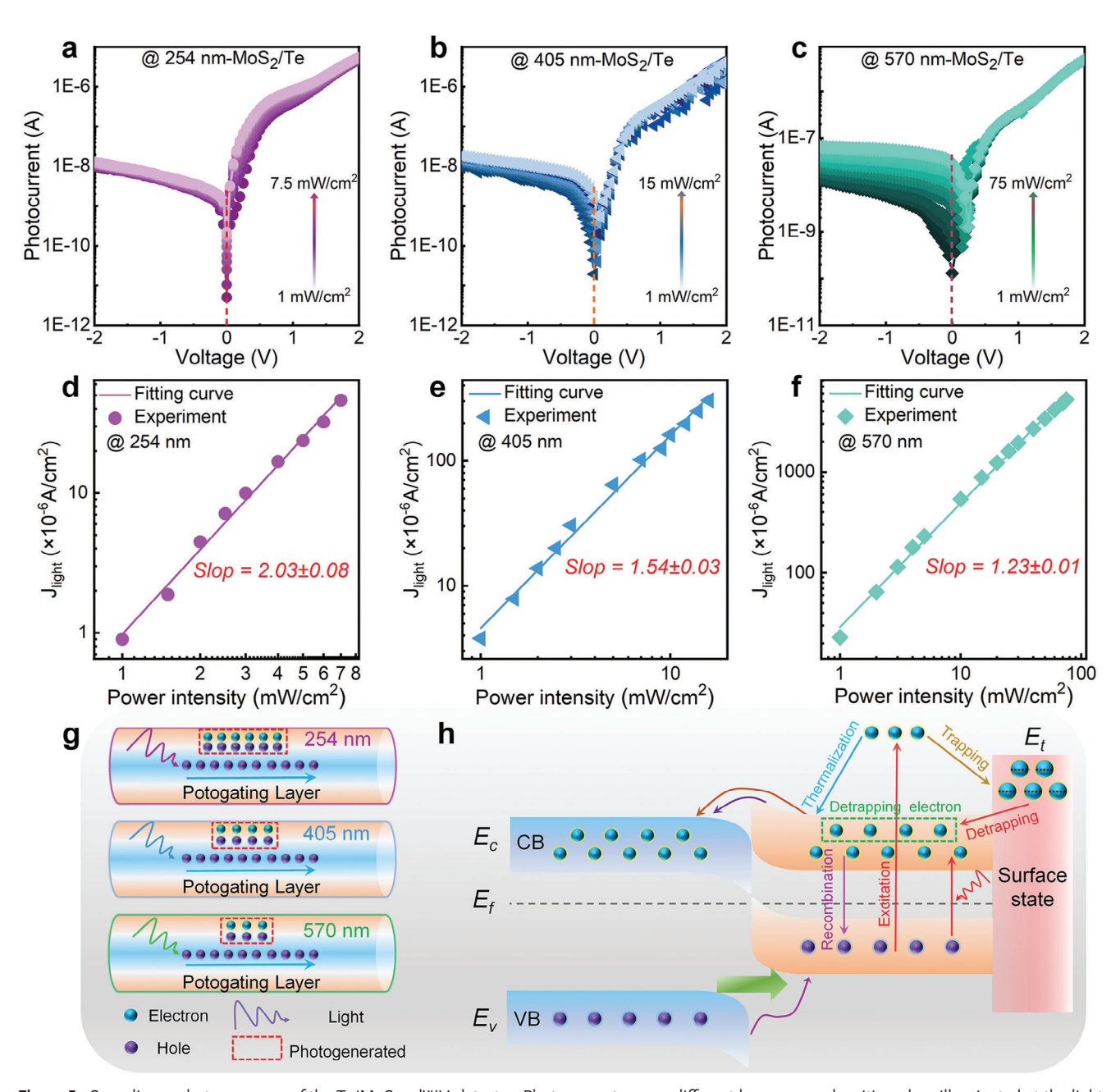


Figure 5. Superlinear photoresponse of the  $Te/MoS_2$  vdWH detector. Photocurrent versus different laser power densities when illuminated at the light wavelength of a) 254, b) 405, and c) 570 nm. d–f) Power law fitting of current density versus incident light intensity at 0 V bias. g) The capability of Te surface-state effects to trap photogenerated electrons as the device is illuminated upon lights at wavelengths 254, 405, and 570 nm, respectively. h) Band diagram showing excitation thermalization, recombination, trapping, and detrapping processes.  $E_c$ ,  $E_v$ ,  $E_f$ , and  $E_t$  represent the conduction band, valence band, Fermi level, and trap level, respectively.

of the Te SCs, the photogenerated hot electrons can cross the potential barrier and then are captured by the surface state defects. Subsequently, the trapped electrons may be released back into the conduction band below the barrier through a thermally activated process. As illustrated in Figure 5g, for the high-energy photons, the excited electrons are easily captured by the surface states, whereas electrons excited by low-energy photons may be blocked by the energy barrier of the trap states. In this case, under 254 nm illumination, the Te surface state defects capture

more photocarriers than those of the light illumination at 405 and 570 nm, respectively. Figure S12 (Supporting Information) shows the electronic band of Te and MoS<sub>2</sub> before contact. The conduction band minimum and the valance band maximum of Te are higher than those of MoS<sub>2</sub>, indicating that the Te/MoS<sub>2</sub> vdWH detector is a type-II band configuration. When the device is irradiated by high-energy photons (Figure 5h), the photogenerated electrons in the Te SC are able to jump into its conduction band. Driven by the built-in electric field, these electrons would

16163028, 0, Downloaded from https://advanced.onlinelibrary.wiley.com/doi/10.1002/adfm.202420359 by Fudan University, Wiley Online Library on [06:032025]. See the Terms and Conditions (https://onlinelibrary.wiley.com/terms

and-conditions) on Wiley Online Library for rules of use; OA articles are governed by the applicable Creative Commons License

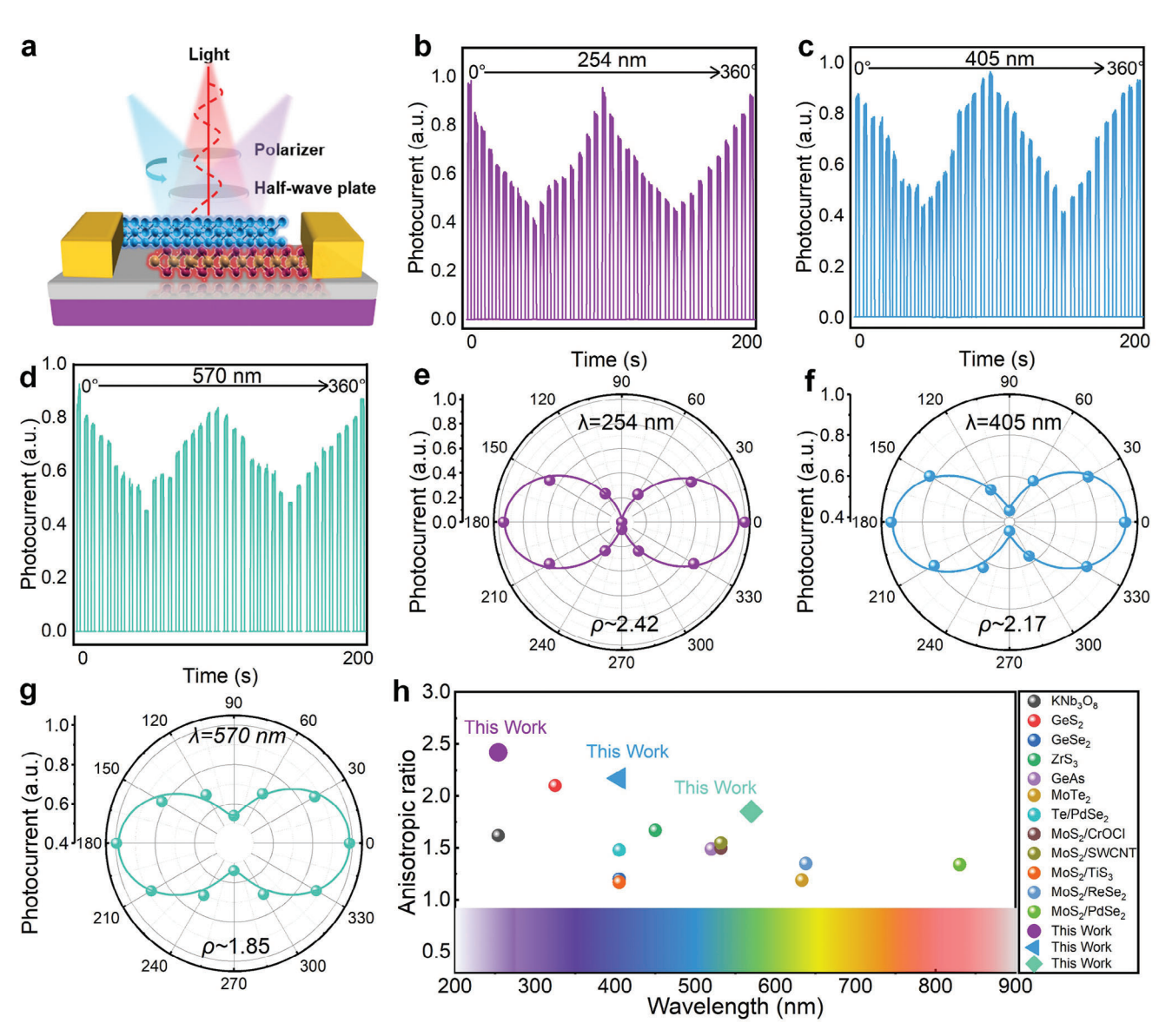


**Figure 6.** a) The schematic of polarization-sensitive Te/  $MoS_2$  photodetector. Polarized photo-switching response of the Te/  $MoS_2$  heterojunction under zero bias for the incident wavelengths of b) 254, c) 405, and d) 570 nm, respectively. Polar diagram of the polarized photoresponsivity under zero bias for the incident wavelengths of e) 254, f) 405, and g) 570 nm, with the corresponding anisotropic ratio 2.42, 2.17, and 1.85, respectively. h) Comparison of the dichroic ratio of the Te/MoS<sub>2</sub> polarization-sensitive photodetector with other low-dimensional material and  $MoS_2$ -based photodetectors.

migrate into the conduction band of  $MoS_2$ . Simultaneously, hot electrons excited by high-energy photons possess sufficient energy to overcome the barrier and are subsequently trapped by surface state defects. The process of electrons being released from defects back into the conduction band is known as detrapping, which requires thermal assistance. Using a thermal imager, we measured the device temperatures when illuminated by the light sources at 254, 405, and 570 nm wavelengths (the optical power intensity  $\approx$ 7.0 mW cm<sup>-2</sup>, Figure S13, Supporting Information). Obviously, the incoming light at 254 nm generates the highest heat, making it easier for electrons trapped in the surface state to separate and transfer to the conduction band on the Te side. The highly conductive surface state of Te and its low contact barrier formed with  $MoS_2$  effectively reduce the interfacial

potential fluctuation. This allows the electrons captured in the Te conduction band to be easily transferred into  $MoS_2$ , which in turn facilitates the generation of superlinear photoresponsive behavior.

Based on the superior broadband optical detection performance of the well-fabricated Te/MoS<sub>2</sub> vdWH detector and the inherent in-plane anisotropic structural properties of 1D Te SCs. The polarization-dependent photoelectric properties are characterized using linearly polarized light as the irradiation source. **Figure 6a** shows the measurement settings for angle-resolved polarized photoresponse. To maintain the self-powered mode of the photodetector, the bias voltage between the source and drain electrodes is kept at 0 V bias. As depicted in Figure 6b–d, by adjusting the on/off state of the light source and rotating the angle of the

16163028, 0, Downloaded from https://advanced.onlinelbtarry.wiley.com/doi/10.1002/adfm.020420359 by Fudau University, Wiley Online Library on [06/03/2025]. Sether Terms and Conditions (https://onlinelibrary.wiley.com/terms-and-conditions) on Wiley Online Library for uses: OA arctices are governed by the applicable Creative Commons Licenses

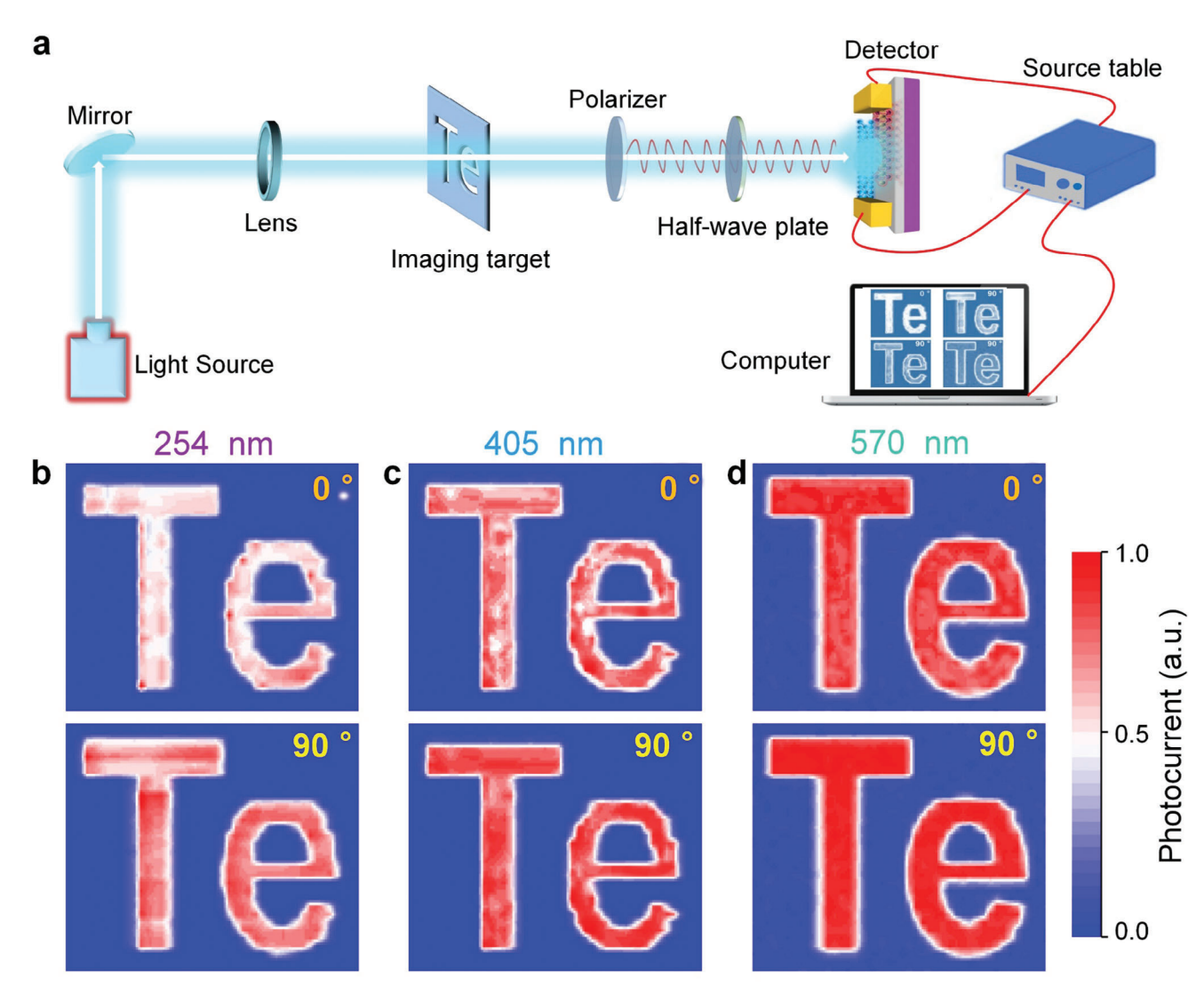


Figure 7. a) Experimental setup of the polarization imaging system. The imaging modes of the letter "Te" at 0° and 90° under wavelengths of b) 254, c) 405, and d) 570, respectively.

half-wave plate, the dynamic photoresponses of the photodetector under light illumination at wavelengths of 254, 405, and 570 nm are recorded, respectively. The device exhibits periodic variations in photocurrent under light irradiation at different wavelengths. The photocurrent reaches its peak at polarization angles of 0° (180°) and its minimum at 90° (270°). The normalized photocurrent polar plots are further shown in Figure 6e-g, which allows us to make the relationship between photocurrent and angle more intuitively. Clearly, the obtained polar plots exhibit similar bi-lobe shapes. The anisotropy ratio of the photodetector, which is defined as  $I_{\text{ph-max}}/I_{\text{ph-min}}$ , exhibits a significant wavelength dependence, reaching 2.42, 2.17, and 1.85 under light illumination at 254, 405, and 570 nm, respectively. In comparison, the anisotropy ratio of the angle-resolved polarized light response cannot be observed in the MoS<sub>2</sub> photodetector (Figure S14, Supporting Information). Compared to the visible light bands of 405 and 570 nm, the larger value at 254 nm can be attributed to the presence of surface state defects within the Te side when 254 nm light illuminates the Te/MoS<sub>2</sub> vdWH device. These defects enable the capture of more photogenerated electrons, resulting in greater gain. The photocarriers are effectively separated under the driven by the built-in electric field. This effectively reduces the probability of compounding of electrons and holes during transport, which significantly improves the polarization performance of the device in the solar blind region. In Figure 6h, the photodetector exhibits excellent polarization characteristics across both solar-blind UV and visible light wavelengths. Its anisotropy ratios are significantly higher than those previously reported MoS<sub>2</sub>-based heterojunctions and other anisotropic low-dimensional materials such as KNb<sub>3</sub>O<sub>8</sub>, GeS<sub>2</sub>, ZrS<sub>3</sub>, etc.<sup>[43,45–55]</sup>

**Figure 7**a depicts the schematic setup for the polarization imaging test, employing fiber lasers operating at wavelengths 254, 405, and 570 nm, respectively. A mask featuring the letter "Te" is positioned behind the light source, serving as the target for the photo imaging. In front of the focusing lens, a polarizer and a half-wave plate are arranged to transform the incoming light

16163028, 0, Downloaded from https://advanced.onlinelbitary.wiley.com/doi/10.1002/adfm.020420359 by Fudau University, Wiley Online Library on [06032025]. Sethe Terms and Conditions (https://onlinelibrary.wiley.com/terms-and-conditions) on Wiley Online Library for Ireles of use; OA articles are governed by the applicable Creative Commons License

www.afm-journal.de

into linearly polarized light, allowing for the adjustment of the polarization direction through the rotation of the half-wave plate. The Te/MoS<sub>2</sub> vdWH photodetector is mounted on a computer-controlled rotating stage, allowing continuous motion and line-by-line scanning of the target imaging object ("Te") under the light. Thus, the Te/MoS<sub>2</sub> device serves as a single sensing pixel. During image sensing, the computer collects photocurrent from the Te/MoS<sub>2</sub> photodetector while simultaneously recording the position data of the object. Finally, the input signal current is converted into an image by the imaging system. Figure 7b–d shows the polarization imaging of the letter "Te" at different wavelengths and two polarization angles of 0° and 90°. The observed distinct polarization differentiation and clear boundaries confirm the powerful polarized light imaging capability of the Te/MoS<sub>2</sub> photodetector.

# 3. Conclusion

In summary, a high-performance p-Te/n-MoS2 vdWH photodetector featuring fast response speed, broadband response, and remarkable polarization photosensitivity, is experimentally exhibited. Importantly, the p-Te/n-MoS<sub>2</sub> detector exhibits a superlinear photoresponse with respect to the wavelengths of incoming lights. The resulting  $\alpha$  values are evaluated to 2.03, 1.54, and 1.23 upon light illumination at 254, 405, and 570 nm, respectively. Benefiting from the superlinear photoresponse, the device demonstrates competitive overall performance with its competitors upon intense light illumination. The experimental results align well with the theoretical computation and analysis, confirming that the delicate integration of 1D Te SCs (high mobility, excellent electrical transport properties, and self-assembled nearsurface photogating layer) is crucial for achieving the superlinear photoresponse. Furthermore, the helical chain structure of 1D Te SCs enables the device to exhibit an adjustable polarization extinction ratio ranging from 2.42 to 1.85 within the solar-blind to visible light wavelength range. This exceptionally efficient lightmatter interaction provides an effective route for Te-related optoelectronic devices operating in harsh environments.

# 4. Experimental Section

Materials Preparation—During the Growth Process, the Formation of Near Surface Defects in Te Is Primarily Influenced by Two Factors: Low-dimensional Te monocrystalline structures with controllable morphology are grown on SiO $_2$ /Si substrates using a physical vapor deposition method. A ceramic boat loaded with pure Te powder (99.99%, 50 mg) is positioned upstream in the tube furnace. It is heated to 450 °C at a rate of 20 °C per minute to encourage volatilization. A SiO $_2$ /Si substrate is placed at the downstream end as a growth surface, and the temperature is maintained at 345 °C. Argon gas (≈40 sccm) is used as the carrier gas to assist in the migration of Te atoms to the substrate. The growth process is maintained for 20 min. The pressure is maintained at ≈60 Pa for the entire process. Upon natural cooling of the tube furnace to room temperature, the product of low-dimensional Te single-crystals is obtained on the substrate.

The first factor is the relatively high growth pressure ( $\approx$ 60 Pa), which results in a shorter mean free path for the vaporized Te atoms. This shortened mean free path leads to collisions among the atoms more frequently, causing disruptions in their orderly deposition on the substrate. As a consequence, defects are formed on the surface of the growing Te material.

The second factor is the combination of elevated temperatures within the growth zone and an ample supply of the precursor material. The high temperature provides the necessary energy for the catalytic oversaturation of the Te source vapor, which is generated from the precursor. When there is an excess of source vapor, it reacts unevenly on the surface of the Te. This uneven reaction promotes the formation of defects, as the excess vapor cannot be accommodated uniformly on the surface, leading to structural irregularities and imperfections. These two factors, high growth pressure, and excessive source vapor, interact to create a conducive environment for the emergence of surface defects in the low-dimensional Te materials grown via physical vapor deposition.

Device Fabrication: First, multilayer MoS2 flakes are mechanically exfoliated from a bulk crystal (SixCarbon Technology Shenzhen) using transparent tape and subsequently transferred onto a Si/SiO2 substrate. This step allows for the isolation of thin layers of MoS<sub>2</sub> for further manipulation and study. Second, vertical stacking of the transferred MoS<sub>2</sub> flakes is achieved using a three-axis robotic arm platform in conjunction with dry transfer techniques employing a micro-manipulator. This precise process ensures accurate alignment and stacking of the MoS<sub>2</sub> layers, creating a vertically aligned heterostructure. Lastly, Ni/Au electrodes (10/50 nm) are deposited onto the Te/MoS<sub>2</sub> heterostructure using the electron beam evaporation technique. The electron beam evaporation process involves heating the Ni and Au source materials in a high-vacuum environment until they reach the point of evaporation. The resulting vapor is then deposited onto the surface of the heterostructure. This technique ensures that the electrodes are uniformly and conformally coated onto the surface, providing reliable electrical contacts for the measurement and characterization of the device's electronic properties.

Characterization and Measurements: Morphological evaluation of samples using scanning electron microscopy (SEM, TESCAN LAYRA3 GM)). The elemental distribution of Te single crystals was analyzed using energy-dispersive X-ray spectroscopy (EDS). High-resolution transmission electron microscopy (HRTEM) was employed to study the crystal structure of the Te single crystals. X-ray diffractograms of PVD-synthesized Te single crystals were obtained by X-ray diffractometer (XRD, Malvern Panalytical, Empyrean). Raman spectra of the Te single crystals were acquired using a Raman spectrometer with a 532 nm laser as the light source. The absorbance of the samples was measured using a micro-area spectrometer. Finally, the prepared photodetectors were tested for their photoelectric properties using a detection system consisting of a xenon lamp, a monochromator, a chopper, a signal generator, a source meter, and a picoammeter.

Calculation Details: The optimization of all models was accomplished through the resolution of the Kohn-Sham equation. The system's state was characterized by the electron density function  $\rho(r)$ , which enabled the calculation of energy, charge transfer, and state density. The process of solving the Kohn-Sham equation involves a self-consistent operation, establishing a convergence criterion for single-atom energy in the self-consistent field at  $10^{-5}$  eV. For the exchange-correlation generic function was opted for the widely-used generalized gradient approximation function. The Perdew-Burke-Ernzerhof function was employed to determine the exchange-correlation energy. The atomic orbitals were computed using the double-numeric basis set with polarization. The convergence criterion for the interatomic interaction force was set to 0.02 Ha nm $^{-1}$ , while the criterion for the maximum atomic displacement was 0.0005 nm. Upon meeting these convergence criteria, the structural optimization was deemed complete.

#### Supporting Information

Supporting Information is available from the Wiley Online Library or from the author.

# Acknowledgements

This study was supported by the National Natural Science Foundation of China (Grant No. 12374257), and the Postgraduate Research & Practice

ADVANCED
FUNCTIONAL
MATERIALS

16163028, 0, Downloaded from https://advanced.onlinelibrary.wiley.com/doi/10.1002/adfm.202420359 by Fudan University, Wiley Online Library on [06/03/2025]. See the Terms and Conditions

(https://onlinelibrary.wiley.com/terms

and-conditions) on Wiley Online Library for rules of use; OA articles are governed by the applicable Creative Commons License

Innovation Program of Jiangsu Province (KYCX24\_0525). The authors acknowledge the facilities in the Center for Microscopy and Analysis at Nanjing University of Aeronautics and Astronautics.

#### **Conflict of Interest**

The authors declare no conflict of interest.

# **Data Availability Statement**

The data that support the findings of this study are available from the corresponding author upon reasonable request.

#### **Keywords**

1D Te single crystal, broadband, photogating effect, polarization sensitive, superlinear photoresponse, Te/MoS<sub>2</sub> van der Waals heterojunction

Received: October 24, 2024 Revised: December 18, 2024 Published online:

- [1] S. Assefa, F. Xia, Y. A. Vlasov, Nature 2010, 464, 80.
- [2] L. Dou, Y. Yang, J. You, Z. Hong, W.-H. Chang, G. Li, Y. Yang, Nat. Commun. 2014, 5, 5404.
- [3] H. Wei, Y. Fang, P. Mulligan, W. Chuirazzi, H.-H. Fang, C. Wang, B. R. Ecker, Y. Gao, M. A. Loi, L. Cao, J. Huang, Nat. Photonics 2016, 10, 222
- [4] X. Lu, P. Jiang, X. Bao, Nat. Commun. 2019, 10, 138.
- [5] L. Lv, F. Zhuge, F. Xie, X. Xiong, Q. Zhang, N. Zhang, Y. Huang, T. Zhai, Nat. Commun. 2019, 10, 3331.
- [6] F. H. L. Koppens, T. Mueller, P. Avouris, A. C. Ferrari, M. S. Vitiello, M. Polini, Nat. Nanotechnol. 2014, 9, 780.
- [7] M. Parker, Nat. Electron. 2024, 7, 628.
- [8] H. Jiang, Y. Chen, W. Guo, Y. Zhang, R. Zhou, M. Gu, F. Zhong, Z. Ni, J. Lu, C.-W. Qiu, W. Gao, Nat. Commun. 2024, 15, 8347.
- [9] T. T. Yan, W. Yang, L. M. Wu, X. S. Fang, J. Mater. Sci. Technol. 2025, 109, 95.
- [10] Y. Chen, X. Peng, W. Qin, S. Li, L. Zhang, Y. Wang, Z. Chen, B. Yang, Y. Yuan, J. He, J. Huang, Y. Lin, Adv. Funct. Mater. 2024, 34, 2403942.
- [11] Y. Zhang, Z. Qin, H. Gao, T. Wang, C. Gao, X. Zhang, W. Hu, H. Dong, Adv. Mater. 2024, 36, 2404309.
- [12] C. Liu, T. Zheng, K. Shu, S. Shu, Z. Lan, M. Yang, Z. Zheng, N. Huo, W. Gao, J. Li, ACS Appl. Mater. Interfaces 2024, 16, 13914.
- [13] X. Y. Lu, K. X. Sun, Y. H. Wang, C. Liu, Y. Y. Meng, X. T. Lang, C. X. Xiao, R. J. Tian, Z. H. Song, Z. W. Zhu, M. Yang, Y. Bai, Z. Y. Ge, Adv. Mater. 2024, 36, 2400852.
- [14] W. Liu, J. Lv, L. Peng, H. Guo, C. Liu, Y. Liu, W. Li, L. Li, L. Liu, P. Wang, S. C. Bodepudi, K. Shehzad, G. Hu, K. Liu, Z. Sun, T. Hasan, Y. Xu, X. Wang, C. Gao, B. Yu, X. Duan, *Nat. Electron.* **2022**, *5*, 281.
- [15] H. Guan, F. Liu, Z. He, H. Xie, M. Xie, Z. Fang, M. Yang, B. Chen, X. Liang, F. Li, Y. Wei, T. Yang, H. Lu, *Laser Photonics Rev.* 2024, 1, 2400445.
- [16] X. Chen, Y. Zhang, R. Tian, X. Wu, Z. Luo, Y. Liu, X. Wang, J. Zhao, X. Gan, Nano Lett. 2023, 23, 1023.
- [17] Y. Zhang, X. Chen, M. Zhang, X. Wu, J. Wang, R. Tian, L. Fang, Y. Zhang, J. Zhao, X. Gan, Adv. Funct. Mater. 2024, 34, 2402957.
- [18] M. Massicotte, P. Schmidt, F. Vialla, K. Watanabe, T. Taniguchi, K. J. Tielrooij, F. H. L. Koppens, *Nat. Commun.* 2016, 7, 12174.

- [19] Y. R. Kim, T. L. Phan, Y. S. Shin, W. T. Kang, U. Y. Won, I. Lee, J. E. Kim, K. Kim, Y. H. Lee, W. J. Yu, ACS Appl. Mater. Interfaces 2020, 12, 10772.
- [20] L. Li, W. Wang, L. Gan, N. Zhou, X. Zhu, Q. Zhang, H. Li, M. Tian, T. Zhai, Adv. Funct. Mater. 2016, 26, 8281.
- [21] W. Wang, Y. Meng, W. Wang, Z. Zhang, P. Xie, Z. Lai, X. Bu, Y. Li, C. Liu, Z. Yang, S. Yip, J. C. Ho, Adv. Funct. Mater. 2022, 32, 2203003.
- [22] V. Klee, E. Preciado, D. Barroso, A. E. Nguyen, C. Lee, K. J. Erickson, M. Triplett, B. Davis, I. H. Lu, S. Bobek, J. McKinley, J. P. Martinez, J. Mann, A. A. Talin, L. Bartels, F. Léonard, *Nano Lett.* 2015, 15, 2612.
- [23] B. Y. Zhang, T. Liu, B. Meng, X. Li, G. Liang, X. Hu, Q. J. Wang, Nat. Commun. 2013, 4, 1811.
- [24] M. Kumar, S. Lim, J. Kim, H. Seo, Adv. Mater. 2023, 35, 2210907.
- [25] W. Li, X.-M. Lu, G.-Q. Li, J.-J. Ma, P.-Y. Zeng, J.-F. Chen, Z.-L. Pan, Q.-Y. He, Appl. Surf. Sci. 2016, 364, 560.
- [26] N. Zhang, G. Zhao, L. Li, P. Wang, L. Xie, B. Cheng, H. Li, Z. Lin, C. Xi, J. Ke, M. Yang, J. He, Z. Sun, Z. Wang, Z. Zhang, C. Zeng, Proc. Natl. Acad. Sci. USA 2020, 117, 11337.
- [27] X. An, F. Liu, Y. J. Jung, S. Kar, Nano Lett. 2013, 13, 909.
- [28] T. Ikari, H. Berger, F. Levy, Mater. Res. Bull. 1986, 21, 99.
- [29] T. Ideue, M. Hirayama, H. Taiko, T. Takahashi, M. Murase, T. Miyake, S. Murakami, T. Sasagawa, Y. Iwasa, Proc. Natl. Acad. Sci. USA 2019, 116, 25530.
- [30] M. Peng, R. Xie, Z. Wang, P. Wang, F. Wang, H. Ge, Y. Wang, F. Zhong, P. Wu, J. Ye, Q. Li, L. Zhang, X. Ge, Y. Ye, Y. Lei, W. Jiang, Z. Hu, F. Wu, X. Zhou, J. Miao, J. Wang, H. Yan, C. Shan, J. Dai, C. Chen, X. Chen, W. Lu, W. Hu, Sci. Adv. 2021, 7, eabf7358.
- [31] J. O. Island, S. I. Blanter, M. Buscema, H. S. J. van der Zant, A. Castellanos-Gomez, Nano Lett. 2015, 15, 7853.
- [32] Y. Yang, X. Peng, H.-S. Kim, T. Kim, S. Jeon, H. K. Kang, W. Choi, J. Song, Y.-J. Doh, D. Yu, Nano Lett. 2015, 15, 5875.
- [33] M. Ámani, C. Tan, G. Zhang, C. Zhao, J. Bullock, X. Song, H. Kim, V. R. Shrestha, Y. Gao, K. B. Crozier, M. Scott, A. Javey, ACS Nano 2018, 12, 7253.
- [34] J. Zhou, G. Zhang, W. Wang, Q. Chen, W. Zhao, H. Liu, B. Zhao, Z. Ni, J. Lu, Nat. Commun. 2024, 15, 1435.
- [35] R. Yan, J. R. Simpson, S. Bertolazzi, J. Brivio, M. Watson, X. Wu, A. Kis, T. Luo, A. R. Hight Walker, H. G. Xing, ACS Nano 2014, 8, 986.
- [36] Q. Zhao, F. Gao, H. Chen, W. Gao, M. Xia, Y. Pan, H. Shi, S. Su, X. S. Fang, J. Li, Mater. Horiz 2021, 8, 3113.
- [37] J. Liu, Q. Hao, H. Gan, P. Li, B. Li, Y. Tu, J. Zhu, D. Qi, Y. Chai, W. Zhang, F. Liu, Laser Photonics Rev. 2022, 16, 2200338.
- [38] Z.-Y. Sun, Y. Li, B. Xu, H. Chen, P. Wang, S.-X. Zhao, L. Yang, B. Gao, X.-M. Dou, B.-Q. Sun, L. Zhen, C.-Y. Xu, Adv. Opt. Mater. 2021, 9, 2100438.
- [39] J. Xiong, Q. Yu, X. Hou, B. Liu, S. Li, H. Deng, Z. Yang, J. Leng, S. Zhu, Y. Sun, Z. Jiang, N. Huo, J. Wu, P. Zhou, Adv. Funct. Mater. 2024, 34, 2314972.
- [40] F. Qin, F. Gao, M. Dai, Y. Hu, M. Yu, L. Wang, W. Feng, B. Li, P. Hu, ACS Appl. Mater. Interfaces 2020, 12, 37313.
- [41] C. Zhao, D. Wang, J. Cao, Z. Zeng, B. Zhang, J. Pan, D. Liu, S. Liu, S. Jiao, T. Chen, G. Liu, X. Fang, L. Zhao, J. Wang, *Nano Res.* 2024, 17, 1864.
- [42] J. Chen, T. Zhang, J. Wang, L. Xu, Z. Lin, J. Liu, C. Wang, N. Zhang, S. P. Lau, W. Zhang, Sci. Adv. 2022, 8, eabn3837.
- [43] P. Wang, Z. Li, X. Xia, J. Zhang, Y. Lan, L. Zhu, Q. Ke, H. Mu, S. Lin, Small 2024, 20, 2401216.
- [44] H. Fang, W. Hu, P. Wang, N. Guo, W. Luo, D. Zheng, F. Gong, M. Luo, H. Tian, X. Zhang, C. Luo, X. Wu, P. Chen, L. Liao, A. Pan, X. Chen, W. Lu, *Nano Lett.* 2016, 16, 6416.
- [45] J. Lai, X. Liu, J. Ma, Q. Wang, K. Zhang, X. Ren, Y. Liu, Q. Gu, X. Zhuo, W. Lu, Y. Wu, Y. Li, J. Feng, S. Zhou, J.-H. Chen, D. Sun, Adv. Mater. 2018, 30, 1707152.



www.advancedsciencenews.com



www.afm-journal.de

16163028, 0, Downloaded from https://advanced.onlinelibrary.wiley.com/doi/10.1002/adfm.202420359 by Fudan University, Wiley Online Library on [06/03/2025]. See the Terms

) on Wiley Online Library for rules of use; OA articles are governed by the applicable Creative Commons License

- [46] Z. Zhou, M. Long, L. Pan, X. Wang, M. Zhong, M. Blei, J. Wang, J. Fang, S. Tongay, W. Hu, J. Li, Z. Wei, ACS Nano 2018, 12, 12416.
- [47] Y. Yang, S.-C. Liu, X. Wang, Z. Li, Y. Zhang, G. Zhang, D.-J. Xue, J.-S. Hu, Adv. Funct. Mater. 2019, 29, 1900411.
- [48] Y. Yan, W. Xiong, S. Li, K. Zhao, X. Wang, J. Su, X. Song, X. Li, S. Zhang, H. Yang, X. Liu, L. Jiang, T. Zhai, C. Xia, J. Li, Z. Wei, Adv. Opt. Mater. 2019, 7, 1900622.
- [49] Y. Ping, H. Long, H. Liu, C. Chen, N. Zhang, H. Jing, J. Lu, Y. Zhao, Z. Yang, W. Li, Adv. Funct. Mater. 2022, 32, 2111673.
- [50] X. Zheng, Y. Wei, X. Zhang, Z. Wei, W. Luo, X. Guo, J. Liu, G. Peng, W. Cai, H. Huang, Adv. Funct. Mater. 2022, 32, 2202658.
- [51] K. Li, C. Du, H. Gao, T. Yin, Y. Yu, W. Wang, J. Materiomics 2022, 8, 1158.
- [52] P.-Y. Huang, H.-J. Chen, J.-K. Qin, L. Zhen, C.-Y. Xu, Nanoscale Adv 2022, 4, 5290.
- [53] T. Lv, X. Huang, W. Zhang, C. Deng, F. Chen, Y. Wang, J. Long, H. Gao, L. Deng, L. Ye, ACS Appl. Mater. Interfaces 2022, 14, 48812.
- [54] F. Chen, G. Liu, Z. Xiao, H. Zhou, L. Fei, S. Wan, X. Liao, J. Yuan, Y. Zhou, ACS Appl. Mater. Interfaces 2023, 15, 16999.
- [55] H. Gao, C. Du, L. Chen, W. Wang, K. Li, Adv. Mater. Interfaces 2022, 9, 2102350.